CryoEM map of *Pseudomonas aeruginosa* PilQ enables structural characterization of TsaP

Matthew McCallum[1,2, †, ‡], Stephanie Tammam[1,†], John L. Rubinstein[1,2,3,*], Lori L. Burrows[4,*], P. Lynne Howell[1,2,*]

[1]Program in Molecular Structure & Function, Peter Gilgan Centre for Research and Learning, The Hospital for Sick Children, Toronto, ON M5G 0A4, Canada.

[2]Department of Biochemistry, University of Toronto, Toronto, ON M5S 1A8, Canada

[3]Department of Medical Biophysics, University of Toronto, Toronto, ON M5G 1l7, Canada.

[4]Department of Biochemistry and Biomedical Sciences and the Michael G. DeGroote Institute for Infectious Disease Research, McMaster University, Hamilton, ON L8S 4K1, Canada.

[*]To whom correspondence should be addressed:

howell@sickkids.ca, lori.burrows@mcmaster.ca, john.rubinstein@utoronto.ca

Lead contact: PLH

[†]These authors contributed equally to this work

[‡]Current address: Department of Biochemistry, University of Washington, Seattle, WA 98195-7350, USA.

ABSTRACT

21
22   The type IV pilus machinery is a multi-protein complex that polymerizes and
23 depolymerizes a pilus fibre used for attachment, twitching motility, phage adsorption, natural
24 competence, protein secretion, and surface-sensing. An outer membrane secretin pore is required
25 for passage of the pilus fibre out of the cell. Herein, the structure of the tetradecameric secretin,
26 PilQ, from the *Pseudomonas aeruginosa* type IVa pilus system was determined to 4.3 Å and 4.4
27 Å resolution in the presence and absence of C_7 symmetric spokes, respectively. The heptameric
28 spokes were found to be the two tandem C-terminal domains of TsaP. TsaP forms a belt around
29 PilQ and while the protein is not essential for twitching motility, over-expression of TsaP triggers
30 a signal cascade upstream of PilY1 leading to cyclic di-GMP up-regulation. These results resolve
31 the identity of the spokes identified with Proteobacterial PilQ homologs and may reveal a new
32 component of the surface-sensing cyclic di-GMP signal cascade.
33

IMPACT STATEMENT

35 The type IV pilus is critical for bacterial virulence. The co-structure of the pilus secretin PilQ and
36 TsaP is determined. Characterization of TsaP implicates it in surface-sensing signal transduction.
37

INTRODUCTION

39   The type IVa pilus (T4aP) facilitates many bacterial functions including attachment,
40 twitching motility, phage adsorption, natural competence, protein secretion, and surface-
41 sensing[1,2]. The surface-sensing role of T4aP is of particular interest due to its involvement in the
42 up-regulation of cyclic di-GMP – the master regulator of biofilm formation[3,4]. Biofilms are of
43 critical medical and industrial importance, as they increase bacterial tolerance of otherwise
44 uninhabitable conditions, antibiotics, and to the immune system[5].
45   The T4aP machinery comprises a cell envelope-spanning multi-protein complex. This
46 machinery polymerizes long thin fibres that attach to surfaces and retract to pull bacteria towards
47 the point of attachment[1,2]. The pilus is a polymer mainly composed of the major subunit, PilA. At
48 the pilus base, the inner membrane protein PilC and cytoplasmic ATPase motors, PilB and PilT,
49 catalyze polymerization and depolymerization, respectively[6,7]. Minor pilins and PilY1 initiate
50 pilus polymerization and are thus thought to localize at the pilus tip[8,9]. The pilus exits the
51 periplasm through an outer membrane pore formed by PilQ oligomers. The PilQ pore is aligned

52 with the motors by a subcomplex of PilM, PilN, PilO, and PilP[10,11]. PilF shuttles PilQ to the outer

53 membrane and facilitates its oligomerization. PilMNOP, PilY1, and PilT are all required for

54 T4aP-mediated surface sensing [12,13]. It is unclear whether other proteins that are part of the T4aP

55 apparatus and interface with PilM, PilN, PilO, and PilP – such as PilQ – are also needed for

56 surface sensing.

57   PilQ and PilF are the secretin and pilotin of the T4aP, respectively. Secretins and their

58 cognate pilotins create outer-membrane channels in various secretion and pilus systems. Secretin

59 oligomers have a unique double-layered β-barrel architecture[14,15]. The outer β-barrel forms a

60 large vestibule that passes though the outer membrane[15]. The inner β-barrel curves inwards to

61 form a gate at the midway point of the secretin β-barrel[15]. Domains N1 and N0 form rings below

62 the β-barrel[15]. PilQ secretins from Proteobacteria, structurally characterized at low resolution,

63 show radial spokes emerging from a central barrel[16-19]. Models of PilQ from *Thermus*

64 *thermophilus* (PilQ^{Tt}) and *Vibrio cholerae* (PilQ^{Vc}) competence pilus systems – which are

65 divergent from Proteobacterial T4aP secretins – were recently built into 7 and 2.7 Å resolution

66 electron cryomicroscopy (cryoEM) maps, respectively [20,21]. These competence secretins lack the

67 lip subdomain and the radial spokes found in T4aP secretins.

68   Structures of the related type II secretion system (T2SS) secretins also have radial

69 spokes[22,23]. These structures were determined at 3-4 Å resolution, permitting modeling of the

70 spoke protein as the T2SS pilotin[22,23]. This finding suggests that the spokes in the T4aP structures

71 could be the T4aP pilotin, PilF. However, PilF is structurally unrelated to the T2SS pilotin, and

72 other studies indicate that the spokes are most likely the protein TsaP[16,19]. 2D class averages of

73 cryoEM particles embedded in purified *Neisseria* sp. membranes show spokes around the PilQ

74 barrel, and these spokes disappear upon deletion of TsaP[16]. Similarly, electron cryotomography

75 of *Myxococcus xanthus* show that density consistent with the location of the spokes around PilQ

76 disappears upon deletion of TsaP[19]. Little is known about the molecular function of TsaP, except

77 that it has a LysM domain characteristic of septal peptidoglycan binding[16]. Neither TsaP nor PilF

78 are not expressed in the same operon as PilQ.

79   We previously resolved a 7.4 Å map of PilQ from *Pseudomonas aeruginosa* (PilQ^{Pa}) with

80 presumed tetradecameric stoichiometry and C_7 symmetric spoke density[18]. Although this was the

81 highest resolution structure of a secretin at that time, it was not sufficient for model building.

82 Herein, our reprocessing of those micrographs with improved image analysis and model-building

83   algorithms yielded three distinct structures of $PilQ^{Pa}$. These maps were of sufficient resolution to

84   enable building of an atomic model. Mass spectrometry revealed the identity of the protein bound

85   in the spoke density to be TsaP, and a TsaP model was readily built into the spoke density. While

86   probing for the function of TsaP, we found that that its overexpression triggers cyclic di-GMP

87   up-regulation upstream of PilY1, implicating a role in the T4aP-dependent surface-sensing signal

88   cascade.

89

90   **RESULTS**

91   **$PilQ^{Pa}$ forms tetradecameric and pentadecameric barrels**

92   We previously resolved a 7.4 Å resolution $PilQ^{Pa}$ cryoEM map[18]. Using the template-

93   based automatic particle selection algorithm implemented in cryoSPARC v.2[24], eight times more

94   particles were selected automatically from the original micrographs than when particle selection

95   was performed manually (**Supplementary Table 1**). *Ab initio* classification followed by

96   heterogeneous particle refinement in 3D revealed three unique classes, with 44 % of particle

97   images classified as C_{14} symmetric barrels with C_7 symmetric radial spokes (**Figure 1A)**, 48 % of

98   particle images classifying as C_{14} symmetric barrels without spokes (**Figure 1B)**, and 8 % as C_{15}

99   symmetric barrels without spokes (**Figure 1C**). Refining the three classes yielded maps at 4.3,

100   4.4, and 6.9 Å resolution, respectively. The distinct C_{14} and C_{15} symmetric maps identified are

101   reminiscent of the finding that the T2SS secretin can have more than one symmetry[25].

102   Local resolution in the barrel of the 4.3 and 4.4 Å maps is estimated to be 3.5 Å. The

103   secondary structure and large side chains were visible in the map and enabled model building of

104   14 $PilQ^{Pa}$ N1 and secretin domains (**Figure 1A**). Although we verified that the N0 and

105   peptidoglycan-binding AMI_N domains of PilQ were present using mass spectrometry analyses

106   (**Supplementary Figure 1**), they could not be modeled, consistent with these domains adopting

107   random orientations relative to the secretin barrel in the absence of the peptidoglycan and the rest

108   of the T4aP apparatus. Protomers of the barrel structure from the spoked barrel map were fit into

109   the maps of the C_{14} and C_{15} barrels without spokes and refined.

110   The final models were compared to co-evolved residues within $PilQ^{Pa}$ homologs as

111   identified by the EVcouplings webserver[26]. Residues in proximity to one another in a structure

112   develop complementary mutations as the protein evolves[27]. These co-evolved residues can be

113   used to independently predict and validate the conformations of proteins[27]. We found a clear

4

114   correlation between the co-evolved residues and the N1 and secretin domains, validating these

115   structures (**Figure 1D**). The sequence of the lip subdomain is not well conserved in PilQ, and the

116   poor sequence alignment in this region yielded fewer co-evolved residues in the lip subdomain

117   (**Figure 1D**).

118

119   **Co-evolved residues are consistent with secretin gate and barrel dynamics**

120   Co-evolved residues not directly supported by the model of PilQ[Pa] were also identified,

121   suggesting dynamics not visualized in the cryoEM maps. There are co-evolved residues between

122   the secretin gate and the secretin barrel (**Figure 1E**), consistent with a swinging gate-like model

123   of secretin gate opening demonstrated recently for the secretin from the type III secretion

124   injectisome, InvG[28]. Residue G577 is located at the proposed hinge of the *P. aeruginosa* PilQ

125   secretin gate (**Figure 1E**). Mutation of the corresponding residue in *M. xanthus* PilQ (G764S)

126   causes vancomycin sensitivity[29] presumably because the hinge of the gate is jammed open

127   permitting entry of the bulky antibiotic across the outer membrane. This hypothesis is supported

128   by the structure of a mutant of the T2SS secretin where the corresponding residue G458 was

129   changed to alanine (G458A)[25]. The G458A T2SS secretin structure reveals a partially open

130   secretin gate[25].

131   Co-evolved residues were also identified at the top of the secretin barrel and near the

132   bottom of the secretin barrel, adjacent to the secretin gate (**Figure 1F**). These co-evolved residues

133   may be consistent with the secretin barrel folding such that the top of the secretin barrel covers

134   the gate-adjacent segment of the secretin. The top of the secretin is hydrophobic (**Figure 1G**),

135   like other secretin structures[15], consistent with this region being the site for outer membrane

136   insertion. Thus, one explanation for these co-evolved residues may be that a folding intermediate

137   positions the top of the secretin barrel to mask these hydrophobic sites prior to membrane

138   insertion (**Figure 1F**). The gate-adjacent section of the secretin barrel is highly conserved

139   (**Figure 1G**) and provides the interface for the spoke density. Once PilQ inserts into the outer

140   membrane and this region becomes exposed, the spoke protein could bind and stabilize the PilQ

141   oligomer.

142

143   **Dynamics in the secretin gates visualized**

5

144   The conformations of the secretin gates in the C_{15}, C_{14}, and spoked C_{14} PilQ^{Pa} barrels are

145   different. While the secretin gate in the C_{15} barrels is perpendicular to the walls of the barrel, the

146   secretin gate in the C_{14} barrel invaginates towards the periplasm. Comparing the C_{15} and C_{14}

147   barrels without spokes, the residues at the center of the secretin gate are displaced by 4 Å (**Figure**

148   **1B-C, Animation 1**). This invagination is likely the result of the 5 Å reduction in diameter of the

149   tetradecameric barrel relative to the pentadecameric form, leaving less room for the gate to

150   extend perpendicularly from the walls of the barrel.

151   Comparing the C_{14} and spoked C_{14} barrels reveals that the secretin gate invaginates by an

152   additional 3 Å in the spoked C_{14} barrel (**Figure 1A-B**). A smaller barrel diameter cannot explain

153   this movement, as the diameters of the C_{14} barrel and spoked C_{14} barrels are identical. Comparing

154   the C_{15}, C_{14}, and spoked C_{14} barrels reveals a pivot point for gate invagination in the secretin

155   barrel adjacent to the secretin gate and the spokes (**Figure 1H-I and Animation 1**). This finding

156   is consistent with the molecules bound at the spokes promoting secretin gate invagination.

157

158   **TsaP co-purifies with PilQ**

159   There are two features in the maps of PilQ^{Pa} that cannot be explained by models of PilQ^{Pa}

160   alone. First are the C_7 symmetric spokes. The spoke density appears to be comprised of 14

161   structurally similar β-roll protein structures that form a belt around PilQ. There are differences in

162   every other β-roll that give the spokes C_7 symmetry (**Figure 1A**). There is also extra density

163   beneath the secretin gate that plugs the small opening in the center of both tetradecameric PilQ

164   barrels – the density is more pronounced in the spoked tetradecameric barrel map (**Figure 1A-B**).

165   The local quality of the map beneath the secretin gate is too poor to identify distinct structural

166   elements. Curiously, there is no evidence of C_{15} barrels with spokes or extra density beneath the

167   secretin gates, hinting at stoichiometry-dependent interactions.

168   To identify the protein(s) that constitute the extra densities, mass spectrometry was

169   performed on the protein sample used for cryoEM grid preparation. Aside from PilQ^{Pa}, the most

170   abundant components are PrpL, PA5122, and TsaP (**Supplementary Table 2, Supplementary**

171   **Figure 2**). TsaP is the protein most likely responsible for the spoke density as it has been shown

172   to be critical for PilQ spoke visualization in *Neisseria* sp. and *M. xanthus*[16,19]. PrpL is an

173   extracellular protease secreted by the T2SS[30,31] and thus unlikely to constitute these densities.

174   PA5122 is an uncharacterized protein with a secretion signal sequence.

6

175

Model building of TsaP reveals unique heptamer structure

176

177   The structure of TsaP is not known; however, TsaP was predicted to have an N-terminal

178   peptidoglycan-binding LysM domain linked by unstructured residues to a C-terminal domain[19].

179   The C-terminal domain of TsaP, henceforth referred to as the CII domain, was predicted to be

180   similar to the C-domain of the flagellar ring-forming component, FlgT[19]. The C-domain of FlgT

181   has a β-roll structure with an extruding finger subdomain[32] and the Phyre[2] structure prediction of

182   TsaP from *P. aeruginosa* is consistent with this fold (**Figure 2A**). To validate this result, TsaP

183   co-evolved residues identified by the EVcouplings webserver[26] were compared with the predicted

184   structure of the TsaP CII domain (**Figure 2B**). The correlations between co-evolved residues and

185   residues close to one another in the CII domain structure prediction provide support for its

186   similarity to the FlgT C-domain. Inspection of TsaP co-evolved residues revealed a duplicate

187   pattern of co-evolved residues preceding the CII domain (**Figure 2B**), consistent with a second

188   domain with a similar structure, henceforth referred to as the CI domain. When the structure of

189   the CI domain segment was predicted[33,34] we found that it was also similar to the FlgT C-domain

190   (**Figure 2A**). This is distinct from previous predictions that identified only a single C-domain in

191   TsaP[19].

192   The β-roll structure and extruding finger subdomain in the CI and CII models can be

193   clearly seen in the spoke density (**Figure 2C**). There is also density consistent with linker

194   residues preceding the CI domain and between the CI and CII domains. In contrast, Phyre[2]

195   predicted structures of PrpL and PA5122 do not fit the size or shape of the spokes. The C-

196   terminal 224 residues of TsaP encompassing the CI and CII domains were therefore modeled and

197   refined into the map. This model reveals that TsaP forms a heptameric ring with C_7 symmetry

198   around $PilQ^{Pa}$ at the midpoint of the barrel where the internal gate is positioned (**Figure 2D**).

199   Each finger subdomain contacts the adjacent C domain to mediate intramolecular CI^n-CII^n

200   interactions and intermolecular CII^n-CI^{n+1} interactions. These finger subdomain interactions

201   correlate with co-evolved residue pairs in TsaP (**Figure 2B**), further validating the model of TsaP

202   built into this map.

203   Each C domain contacts a separate PilQ protomer. The buried surface area of the TsaP-

204   PilQ interaction is 2924 Å^2 per TsaP protomer, or 20468 Å^2 for the entire 7:14 TsaP-PilQ

205   interaction. The buried surface area of the TsaP-TsaP oligomeric interface is 913 Å^2. The larger

7

206   buried surface area of the TsaP-PilQ interface compared with the TsaP-TsaP oligomeric interface

207   hints that the PilQ interaction may help facilitate TsaP oligomerization.

208

Overexpression of TsaP triggers cyclic di-GMP signalling

210   *tsaP* mutants have a 40 % defect in twitching motility, which can be complemented *in*

211   *trans* by leaky expression from *tsaP* under an arabinose-inducible promotor without the addition

212   of arabinose (**Figure 3A**). We previously reported finding no obvious defect in twitching motility

213   with the *tsaP* mutant[18]; this was likely the result of a limited number of replicates combined with

214   the modest phenotype. Compared to the vector control, a 66 % defect in twitching motility is

215   observed in wild-type *P. aeruginosa* or the *tsaP* mutant complemented with *tsaP* when induced

216   with 0.1 % (w/v) arabinose – henceforth referred to as over-expressed TsaP (**Figure 3B**) –

217   consistent with both deletion and over-expression of TsaP impairing twitching motility.

218   We also assessed the propensity of *tsaP* mutants and TsaP-overexpressing *P. aeruginosa*

219   to form biofilms, using a Congo red dye uptake assay. Congo red binds to the Pel polysaccharide

220   in *P. aeruginosa* biofilms, leading to red colonies and a small clear halo around the colonies

221   where the dye has been taken up[35,36]. We found that the *tsaP* deletion mutant is indistinguishable

222   from wild-type *P. aeruginosa* (**Figure 3B**)*.* However, TsaP overexpression in wild type or the

223   *tsaP* mutant leads to red colonies surrounded by pronounced clearing (**Figure 3B**), consistent

224   with the over-expression of TsaP leading to increased biofilm formation.

225   To look at other surface-associated phenotypes, we assessed the propensity of TsaP

226   overexpressing *P. aeruginosa* to secrete proteases using a casein proteolysis assay. Hydrolysis of

227   casein by extracelluar proteases leads to clear halos around protease- secreting colonies on solid

228   skim milk media[37]. Clear halos form around wild-type *P. aeruginosa* and the *tsaP* deletion

229   mutant; however, no halos form around TsaP over-expressing colonies (**Figure 3B**), consistent

230   with its over-expression decreasing extracellular protease secretion.

231   Reduced extracellular protease secretion, decreased twitching motility zones, and

232   increased biofilm formation are all associated with cyclic di-GMP induction[4,38-40]. Measurement

233   of luciferase expression from a cyclic di-GMP sensitive promotor verified that TsaP

234   overexpression increases cellular cyclic di-GMP concentrations (**Figure 3C**). Growth curves

235   confirmed that increased luciferase expression is not a result of increased cell growth (**Figure**

8

236   **3C**). These results are consistent with TsaP over-expression up-regulating the production of

237   cyclic di-GMP.

238

TsaP signalling occurs upstream of PilY1

240   We probed the dependency of cyclic di-GMP signal upregulation caused by TsaP-

241   overexpression on other T4aP proteins. Surprisingly, deletion of PilQ or the PilQ pilotin, PilF,

242   did not prevent TsaP over-expression from increasing Congo-red dye uptake (**Figure 3D**). This

243   indicates that PilQ is not downstream of TsaP in this signal cascade. Like TsaP, PilY1 over-

244   expression in *trans* can trigger increased cyclic di-GMP production[12]. Deleting the *pilMNOP*

245   genes blocks cyclic di-GMP induction upon PilY1 over-expression[12]. When TsaP was over-

246   expressed in a *pilY1* deletion mutant, there was decreased Congo-red dye uptake, consistent with

247   TsaP over-expression inducing a signal cascade that proceeds through PilY1 (**Figure 3D**).

248   Likewise, TsaP over-expression in *pilN*, *pilO*, or *pilP* mutants resulted in less Congo red dye

249   uptake (**Figure 3D**). These results are consistent with TsaP over-expression triggering a T4aP-

250   related cyclic di-GMP signal transduction pathway.

251

DISCUSSION

253   We determined the structure of PilQ alone and bound to TsaP, and found that TsaP over-

254   expression leads to increased expression of cyclic di-GMP, upstream of PilY1. Our results

255   resolve the identity of the spokes identified in Proteobacterial PilQ cryoEM densities and may

256   reveal a new component of the surface-sensing signal cascade.

257   Where most secretins are bound by their cognate pilotin around the periphery of the

258   secretin barrel adjacent to the secretin gate, we found PilQ[Pa] is bound by TsaP. Unlike pilotins,

259   TsaP is not essential for PilQ assembly or twitching motility[16,18,19]. Where and how the pilotin

260   PilF interacts with PilQ remains an open question, although one possibility is that TsaP replaces

261   PilF after insertion of PilQ into the outer membrane. We identified co-evolved residues that are

262   consistent with the TsaP-binding region of PilQ interacting with the hydrophobic membrane-

263   interacting interface. This hints at a model of PilQ membrane insertion in which secretin

264   monomers initially fold onto themselves, with the TsaP-binding site occluding the hydrophobic

265   membrane insertion site. Binding by pilotins to the TsaP-binding site might then promote the

266   insertion of PilQ into the membrane, rationalizing the necessity of pilotins for secretin assembly

9

267   and localization. If this were the case, after outer-membrane insertion of PilQ, PilF could be

268   replaced by TsaP.

269   It seems likely that TsaP and PilQ are tightly associated, as the buried surface area of the

270   TsaP-PilQ interaction is enormous (20468 Å^2) and the complex is stable in detergent. It is

271   nonetheless possible that some of the TsaP rings were removed during the purification, as only

272   about half of the purified PilQ particles have TsaP associated with them. In this case, PilQ

273   partially bound by TsaP might be expected, but only PilQ entirely bound by TsaP or without

274   TsaP were identified in cryoEM 3D classes. Alternatively, there may be a population of free PilQ

275   oligomers representing an intermediate state between PilQ-PilF and PilQ-TsaP complexes.

276   The structure of PilQ was determined in two distinct stoichiometries. Interestingly, only

277   the tetradecameric form is bound by TsaP and had the unidentified secretin gate plug. The 2:1

278   PilQ:TsaP configuration necessitates binding of only even-numbered PilQ stoichiometries. It may

279   be that TsaP recognizes or selects for specific secretin stoichiometries. Selecting particular

280   secretin stoichiometries may improve the efficiency of T4aP function, consistent with the

281   moderate twitching motility defect of the TsaP-deletion mutant.

282   In addition to influencing the quaternary structure of PilQ, TsaP binding may alter its

283   tertiary structure. Comparing the different PilQ structures revealed a pivot point for secretin gate

284   invagination adjacent to the spokes, consistent with TsaP binding influencing this process. Thus,

285   a plausible role for TsaP may be in modifying secretin-gate invagination. The consequences of

286   this are not clear, but the gate could then interact with the pilus initiation complex of minor pilins

287   and PilY1 and/or the unidentified secretin gate plug.

288   TsaP could also be involved with larger-scale secretin movements. For example, PilQ

289   adopts distinct open and closed states depending on whether the pilus fibre occupies the central

290   channel the T4aP[19,20]. Compared to T4aP maps obtained by electron cryotomography in which

291   the pilus fibre does not occupy the T4aP, the OM in the piliated state has moved 20 Å away from

292   PilP and the peptidoglycan[19]. Although the secretin domain is embedded in the OM, the AMI_N

293   and N0 domains of PilQ bind peptidoglycan and PilP, respectively[41]. This suggests that PilQ

294   must extend and contract 20 Å between the piliated and non-piliated states. As TsaP binds to both

295   the peptidoglycan and secretin domain of PilQ, TsaP binding could modulate secretin opening.

296   For example, TsaP could act as an elastic band between the peptidoglycan and outer-membrane

297   components of PilQ, keeping PilQ contracted and the T4aP closed in the absence of an assembled

298   pilus. The predicted disordered residues between the LysM and CI/CII domains could afford

299   TsaP the elasticity required for this action.

300   Alternatively, instead of modulating PilQ structure, TsaP may sense PilQ conformations

301   and relay this information as a part of a signal cascade. However, while TsaP over-expression

302   triggers the cyclic di-GMP signal cascade, it does so independently of PilQ. This is curious as

303   PilQ provides the only known physical contact between TsaP and PilN, PilO, and PilP – which

304   are important for inducing cyclic di-GMP production. It may be that there is a PilQ-independent

305   signal transduction pathway from TsaP to PilY1 and PilNOP. Alternatively, over-expressing

306   TsaP may force a signalling event that is typically dependent on PilQ. As TsaP has a

307   peptidoglycan-binding LysM domain, overexpression might place strain on the peptidoglycan

308   that resembles what happens during surface interactions, leading to cyclic di-GMP induction. In

309   the absence of a known trigger for the signalling cascade upstream of TsaP, it is not clear what

310   role TsaP plays in the surface-sensing signal cascade under native expression conditions.

311   Nonetheless, knowing that TsaP over-expression can trigger the cyclic di-GMP signal cascade

312   upstream of PilY1 will be useful in identifying other key players in the surface sensing signal

313   cascade.

314

315   **METHODS**

316   **Cloning and mutagenesis**

317   TsaP from *P. aeruginosa* PAO1 was PCR amplified from genomic DNA using primers

318   TsaP_fwd and TsaP_rev (**Supplementary Table 3**), digested with KpnI and XbaI, and cloned into

319   pBADGr to create pBADGr:*tsaP* for arabinose inducible expression of TsaP. Plasmid sequences

320   were verified by TCAG sequencing facilities (The Hospital for Sick Children, Canada).

321

322   **TsaP Deletion**

323   A gene deletion allele was ordered from BioBasic and subcloned into pEX18Gm at the

324   BamHI site producing pEX18Gm_*tsaP*. Clones were confirmed by digest and DNA sequencing

325   (TCAG, The Hospital for Sick Children). The pEX18Gm_*tsaP* construct was transformed into

326   chemically competent SM10 *E. coli* cells, colonies containing pEX18Gm_*tsaP* were mated with

327   mPAO1 using a method described elsewhere[42]. Briefly, after mating *P. aeruginosa* was selected

328   for by growth on LB agar plates containing 25 µg/ml triclosan (Sigma) followed by selection of

329   the merodiploid strains on VBMM agar containing 30 μg/ml gentamicin. Counter selection to

330   resolve the merodiploids was performed on 1.5 % agar plates with 10 g/L tryptone, 5 g/L yeast

331   extract, and 15% (wt/vol) sucrose. The deletion was verified by the absence of a PCR product using

332   primers TsaP_fwd and TsaP_rev.

333

334   **Phenotypic characterizations**

335   *P. aeruginosa* PAO1 with and without deletion mutations of *tsaP*, *pilN*, *pilO*, *pilP*, *pilQ*,

336   *pilY1* were electroporated with pBADGr or pBADGr:tsaP. *P. aeruginosa* PAO1 with and without

337   deletion mutations of *tsaP* were also electroporated with pBADGr:tsaP.

338   Twitching assays were performed as described previously[43,44] except that assays were

339   performed in 150 mm by 15 mm petri polystyrene dishes (Fisher Scientific) with 30 μg/ml

340   gentamicin for 18 h at 37 °C. After this incubation, the agar was then carefully discarded and the

341   adherent bacteria were stained with 1 % (w/v) crystal violet dye, followed by washing with

342   deionized water to remove unbound dye. Twitching zone areas were measured using ImageJ

343   software[45]. Twitching motility assays were performed in six replicates.

344   For Congo-red dye binding assays, cells were grown in 0.5 mL of lysogeny broth (LB) with

345   30 μg/ml gentamicin for 16 h at 37 °C while shaking. Cultures were normalized to an OD at 600

346   nm of 0.1 and then 3 μl of culture was spotted onto Congo red plates (1% (wt/vol) Tryptone, 1%

347   (wt/vol) agar, 0.004% (wt/vol) congo red, and 0.0015% (wt/vol) Coomassie Brilliant Blue R250,

348   and either 0, 0.01, or 0.1% L-arabinose) with the appropriate antibiotic, and grown for 24-36 h at

349   37 °C.

350   Extracellular proteases were assayed using skim milk plates (1% wt/vol agar, 1% wt/vol

351   skim milk powder, and either 0, 0.01, or 0.1% L-arabinose) with the appropriate antibiotic, using

352   the same normalized cultures used for the Congo red binding assays. 3 μl of culture was spotted

353   on a plate and incubated for 16 hrs at 37 °C. All plates were scanned using an Epson Perfection

354   4990 scanner and Epson Scan software.

355   For luciferase expression, cells previously electroporated with pBADGr, pBADGr::tsaP

356   and pBADGr::tsaP mutant constructs were electroporated with pMS402:PcdrA. Cells were grown

357   in 0.5 mL of lysogeny broth (LB) with 30 μg/ml gentamicin and 150 μg/ml kanamycin for 16 h at

358   37 °C while shaking. Cultures were normalized to OD600 of 0.1 and diluted 10x into fresh LB

359   broth containing 30 μg/ml gentamicin, 105 μg/ml kanamycin and either 0, 0.01% or 0.1% L-

12

360   arabinose in a 384 well plate (Corning, 3821). All samples were done in triplicate. Growth and

361   luciferase activity were monitored over a 16-hour period in a Synergy Neo2 plate reader (BioTek

362   Instruments). Data was analyzed and plotted using Prism 8 (Graph Pad).

363

364   **Plotting the residues at the packing unit interface**

365   CMview[46] was used to identify residues that are near one another. The contact type was set

366   to 'ALL' (i.e. every atom available in the structure) and the distance cut-off was set to 8 Å. To

367   identify residues that are near one another in PilQ monomers, the CI domain of TsaP (residues 126-

368   211), or the CII domain of TsaP (residues 235-324), these structure segments were loaded

369   separately. To identify intra-molecular CI to CII residues that are near each other in TsaP, full-

370   length TsaP was loaded. To identify inter-molecular residues that are near one another, two

371   adjacent PilQ protomers were loaded together, or the CI domain and CII domains from two adjacent

372   protomers were loaded together.

373

374   **Identifying evolutionarily-coupled residues**

375   The TsaP and PilQ[Pa] amino acid sequences were analyzed using the EVcouplings

376   webserver[26] with default parameters. Homologs were identified, aligned, and analyzed – in total,

377   2642 and 11302 for TsaP and PilQ, respectively. There was poor alignment quality in the lip

378   subdomain of PilQ (residues 481-531) so few evolutionarily-coupled residue pairs were discovered

379   in the lip subdomain. Only residue pairs with a probability score greater than 0.845 or 0.985 were

380   included in subsequent analysis, for TsaP and PilQ, respectively. To better understand the

381   significance of these evolutionarily coupled residues, they were compared to the residues that are

382   near one another identified in CMview.

383

384   **CryoEM analysis**

385   As previously described for this dataset[18], cryoEM data was collected as movies (30 frames

386   over 15 sec) with a FEI Tecnai F20 electron microscope operating at 200 kV and equipped with a

387   Gatan K2 Summit direct detector camera. The exposure rate was 5 electrons/pixel/s with a

388   calibrated pixel size of 1.45 Å/pixel. Previously, movie frames had been aligned with

389   alignframes_lmbfgs[47] and then individual movie frames were discarded for data storage purposes;

390   this prevented exposure weighting and individual particle motion correction herein. Further image

391   processing here was performed in cryoSPARC v2.8.0[24] (**Supplementary Table 1**). CTF

392   parameters were estimated from the average of aligned frames with CTFFIND4[48] within

393   cryoSPARC and individual particle motion correction and exposure weighting was done with an

394   implementation of alignparts_lmbfgs[47] within cryoSPARC. Initial 2D class averages were

395   generated with manually selected particle images; these class averages were then used to select

396   more particle images. Particle images were extracted in 256×256 pixel boxes then subjected to 2D

397   classification. For the purposes of 3D classification, particle images contributing to 2D classes

398   without high-resolution features were removed. *Ab initio* reconstruction was performed using two

399   classes, revealing barrels and spoked-barrels. The particles contributing to the barrels without

400   spokes were used for an additional round of *ab initio* reconstruction with two classes, revealing an

401   additional class with wider barrels. The spoked barrels, the barrels without spokes, and the wider

402   barrels without spokes were then used as initial models for heterogeneous refinement; particles

403   from 3D classes that did not converge at this stage were removed. Particles from distinct 3D classes

404   were then subjected to non-uniform refinement[49]. The resulting fourier shell correlations for the

405   4.3 and 4.4 Å maps are unusual as there is a flat region between ~7 Å and ~5 Å. This likely arises

406   from the diffuse density from the detergent layer and the N-terminal domains disordered relative

407   to the secretin of PilQ. However, the clear features from the beta-barrels support the resolution

408   estimates for the maps

409

410   A molecular model could be built using Coot[50] into the spoked barrel map using the

411   structures of FlgT and GspD[25,32] as guides for TsaP and PilQ, respectively. Molecular models for

412   the maps of barrels without spokes were built by fitting the PilQ protomers built into the spoked

413   barrel map in Coot[50]. These models were refined against the maps in Phenix-Refine[51] with

414   reference model restraints to the spoked barrel PilQ structures. While side-chains were used to

415   ensure the models made biological sense during model building, they were ultimately removed as

416   the map quality did not justify them being modeled.

417

418

424

425

426   **REFERENCES**

427   1.   McCallum, M., Burrows, L.L. & Howell, P.L. The Dynamic Structures of the Type IV
428   Pilus. *Microbiol Spectrum* **7**(2019).

429   2.   Craig, L., Forest, K.T. & Maier, B. Type IV pili: dynamics, biophysics and functional
430   consequences. *Nat Rev Microbiol* **17**, 429-440 (2019).

431   3.   Chang, C.Y. Surface Sensing for Biofilm Formation in Pseudomonas aeruginosa. *Front*
432   *Microbiol* **8**, 2671 (2017).

433   4.   Valentini, M. & Filloux, A. Biofilms and Cyclic di-GMP (c-di-GMP) Signaling: Lessons
434   from Pseudomonas aeruginosa and Other Bacteria. *J Biol Chem* **291**, 12547-55 (2016).

435   5.   Mah, T.F. & O'Toole, G.A. Mechanisms of biofilm resistance to antimicrobial agents.
436   *Trends Microbiol* **9**, 34-9 (2001).

437   6.   McCallum, M., Tammam, S., Khan, A., Burrows, L.L. & Howell, P.L. The molecular
438   mechanism of the type IVa pilus motors. *Nat Commun* **8**, 15091 (2017).

439   7.   McCallum, M. et al. Multiple conformations facilitate PilT function in the type IV pilus.
440   *Nat Commun* **10**, 5198 (2019).

441   8.   Marko, V.A., Kilmury, S.L.N., MacNeil, L.T. & Burrows, L.L. Pseudomonas aeruginosa
442   type IV minor pilins and PilY1 regulate virulence by modulating FimS-AlgR activity.
443   *PLoS Pathog* **14**, e1007074 (2018).

444   9.   Nguyen, Y. et al. Pseudomonas aeruginosa minor pilins prime type IVa pilus assembly
445   and promote surface display of the PilY1 adhesin. *J Biol Chem* **290**, 601-11 (2015).

446   10.   McCallum, M. et al. PilN Binding Modulates the Structure and Binding Partners of the
447   Pseudomonas aeruginosa Type IVa Pilus Protein PilM. *J Biol Chem* **291**, 11003-15
448   (2016).

449   11.   Tammam, S. et al. PilMNOPQ from the Pseudomonas aeruginosa type IV pilus system
450   form a transenvelope protein interaction network that interacts with PilA. *J Bacteriol* **195**,
451   2126-35 (2013).

452   12.   Luo, Y. et al. A hierarchical cascade of second messengers regulates Pseudomonas
453   aeruginosa surface behaviors. *mBio* **6**(2015).

454   13.   Persat, A., Inclan, Y.F., Engel, J.N., Stone, H.A. & Gitai, Z. Type IV pili
455   mechanochemically regulate virulence factors in Pseudomonas aeruginosa. *Proc Natl*
456   *Acad Sci U S A* **112**, 7563-8 (2015).

457   14.   Filloux, A. & Voulhoux, R. Multiple Structures Disclose the Secretins' Secrets. *J*
458   *Bacteriol* **200**(2018).

459   15.   Worrall, L.J. et al. Near-atomic-resolution cryo-EM analysis of the Salmonella T3S
460   injectisome basal body. *Nature* **540**, 597-601 (2016).

461   16.   Siewering, K. et al. Peptidoglycan-binding protein TsaP functions in surface assembly of
462   type IV pili. *Proc Natl Acad Sci U S A* **111**, E953-61 (2014).

463   17.   Collins, R.F. et al. Structure of the Neisseria meningitidis outer membrane PilQ secretin
464   complex at 12 A resolution. *J Biol Chem* **279**, 39750-6 (2004).

18. Koo, J., Lamers, R.P., Rubinstein, J.L., Burrows, L.L. & Howell, P.L. Structure of the Pseudomonas aeruginosa Type IVa Pilus Secretin at 7.4 A. *Structure* **24**, 1778-1787 (2016).

19. Chang, Y.W. et al. Architecture of the type IVa pilus machine. *Science* **351**, aad2001 (2016).

20. Weaver, S.J., Sazinsky, M.H., Dalia, T.N., Dalia, A.B. & Jensen, G.J. CryoEM structure of the Vibrio cholerae Type IV competence pilus secretin PilQ. *bioRxiv* (2020).

21. D'Imprima, E. et al. Cryo-EM structure of the bifunctional secretin complex of Thermus thermophilus. *Elife* **6**, e30483 (2017).

22. Yin, M., Yan, Z. & Li, X. Structural insight into the assembly of the type II secretion system pilotin-secretin complex from enterotoxigenic Escherichia coli. *Nat Microbiol* **3**, 581-587 (2018).

23. Chernyatina, A.A. & Low, H.H. Core architecture of a bacterial type II secretion system. *Nat Commun* **10**, 5437 (2019).

24. Punjani, A., Rubinstein, J.L., Fleet, D.J. & Brubaker, M.A. cryoSPARC: algorithms for rapid unsupervised cryo-EM structure determination. *Nat Methods* **14**, 290-296 (2017).

25. Yan, Z., Yin, M., Xu, D., Zhu, Y. & Li, X. Structural insights into the secretin translocation channel in the type II secretion system. *Nat Struct Mol Biol* **24**, 177-183 (2017).

26. Marks, D.S. et al. Protein 3D structure computed from evolutionary sequence variation. *PLoS One* **6**, e28766 (2011).

27. de Juan, D., Pazos, F. & Valencia, A. Emerging methods in protein co-evolution. *Nat Rev Genet* **14**, 249-61 (2013).

28. Hu, J. et al. Cryo-EM analysis of the T3S injectisome reveals the structure of the needle and open secretin. *Nat Commun* **9**, 3840 (2018).

29. Nudleman, E., Wall, D. & Kaiser, D. Polar assembly of the type IV pilus secretin in Myxococcus xanthus. *Mol Microbiol* **60**, 16-29 (2006).

30. Wilderman, P.J. et al. Characterization of an endoprotease (PrpL) encoded by a PvdS-regulated gene in Pseudomonas aeruginosa. *Infect Immun* **69**, 5385-94 (2001).

31. Michel, G.P., Durand, E. & Filloux, A. XphA/XqhA, a novel GspCD subunit for type II secretion in Pseudomonas aeruginosa. *J Bacteriol* **189**, 3776-83 (2007).

32. Terashima, H. et al. Insight into the assembly mechanism in the supramolecular rings of the sodium-driven Vibrio flagellar motor from the structure of FlgT. *Proc Natl Acad Sci U S A* **110**, 6133-8 (2013).

33. Kelley, L.A., Mezulis, S., Yates, C.M., Wass, M.N. & Sternberg, M.J. The Phyre2 web portal for protein modeling, prediction and analysis. *Nat Protoc* **10**, 845-58 (2015).

34. Yang, J. et al. The I-TASSER Suite: protein structure and function prediction. *Nat Methods* **12**, 7-8 (2015).

35. Jones, C.J. & Wozniak, D.J. Congo Red Stain Identifies Matrix Overproduction and Is an Indirect Measurement for c-di-GMP in Many Species of Bacteria. *Methods Mol Biol* **1657**, 147-156 (2017).

36. Vasseur, P., Vallet-Gely, I., Soscia, C., Genin, S. & Filloux, A. The pel genes of the Pseudomonas aeruginosa PAK strain are involved at early and late stages of biofilm formation. *Microbiology* **151**, 985-997 (2005).

37. Sokol, P.A., Ohman, D.E. & Iglewski, B.H. A more sensitive plate assay for detection of protease production by Pseudomanas aeruginosa. *J Clin Microbiol* **9**, 538-40 (1979).

511 38. Ravichandran, A., Ramachandran, M., Suriyanarayanan, T., Wong, C.C. & Swarup, S.
512   Global Regulator MorA Affects Virulence-Associated Protease Secretion in Pseudomonas
513   aeruginosa PAO1. *PLoS One* **10**, e0123805 (2015).
514 39. Lopez-Baena, F.J., Vinardell, J.M. & Medina, C. Regulation of Protein Secretion Systems
515   Mediated by Cyclic Diguanylate in Plant-Interacting Bacteria. *Front Microbiol* **10**, 1289
516   (2019).
517 40. Jain, R., Behrens, A.J., Kaever, V. & Kazmierczak, B.I. Type IV pilus assembly in
518   Pseudomonas aeruginosa over a broad range of cyclic di-GMP concentrations. *J Bacteriol*
519   **194**, 4285-94 (2012).
520 41. Berry, J.L. et al. Structure and assembly of a trans-periplasmic channel for type IV pili in
521   Neisseria meningitidis. *PLoS Pathog* **8**, e1002923 (2012).
522 42. de Lorenzo, V. & Timmis, K.N. Analysis and construction of stable phenotypes in gram-
523   negative bacteria with Tn5- and Tn10-derived minitransposons. *Methods Enzymol* **235**,
524   386-405 (1994).
525 43. Ha, D.G., Kuchma, S.L. & O'Toole, G.A. Plate-based assay for swarming motility in
526   Pseudomonas aeruginosa. *Methods Mol Biol* **1149**, 67-72 (2014).
527 44. Turnbull, L. & Whitchurch, C.B. Motility assay: twitching motility. *Methods Mol Biol*
528   **1149**, 73-86 (2014).
529 45. Schneider, C.A., Rasband, W.S. & Eliceiri, K.W. NIH Image to ImageJ: 25 years of
530   image analysis. *Nat Methods* **9**, 671-5 (2012).
531 46. Vehlow, C. et al. CMView: interactive contact map visualization and analysis.
532   *Bioinformatics* **27**, 1573-4 (2011).
533 47. Rubinstein, J.L. & Brubaker, M.A. Alignment of cryo-EM movies of individual particles
534   by optimization of image translations. *J Struct Biol* **192**, 188-95 (2015).
535 48. Rohou, A. & Grigorieff, N. CTFFIND4: Fast and accurate defocus estimation from
536   electron micrographs. *J Struct Biol* **192**, 216-21 (2015).
537 49. Punjani, A., Zhang, H., Fleet D. J. Non-uniform refinement: Adaptive regularization
538   improves single particle cryo-EM reconstruction. *bioRxiv* (2019).
539 50. Casanal, A., Lohkamp, B. & Emsley, P. Current Developments in Coot for
540   Macromolecular Model Building of Electron Cryo-microscopy and Crystallographic
541   Data. *Protein Sci* (2019).
542 51. Afonine, P.V. et al. Real-space refinement in PHENIX for cryo-EM and crystallography.
543   *Acta Crystallogr D Struct Biol* **74**, 531-544 (2018).
544
545

546 **Figure Legends**

547 **Figure 1. Electron cryomicroscopy of PilQ from *P. aeruginosa* reveals multiple conformers.**

548 **A-C,** Map (upper left) and model (upper right) of PilQ[Pa] (coloured) with additional spoke and

549 plug density (black). Top (top), side (middle), and cross section (bottom) views are shown. **A,**

550 Map and model of spoked tetradecameric PilQ[Pa] (purple). **B,** Map and model of tetradecameric

551 PilQ[Pa] without spokes (teal). **C,** Map and model of pentadecameric PilQ[Pa] (orange). **D,**

552 Evolutionarily coupled residues in PilQ (gray) are compared with the structure of PilQ[Pa]. Residue

553   pairs that are within 8 Å of each other in the tertiary structure of PilQ[Pa] are shown (black).

554   Residue pairs that are within 8 Å of each other between PilQ[Pa] protomers are also shown (gold).

555   Specific evolutionarily coupled residues that are not supported by the PilQ[Pa] structure are noted

556   with coloured arrows: G554-P635 (yellow), E663-A624 (red), T538-E652 (green), L545-T653

557   (magenta), and L546-V457 (blue). **E**, Location of the G554-P635 and E663-A624 residue pairs,

558   as well as hinge residue G577 (asterisk), on a cross section of PilQ[Pa] (left) and a model for

559   secretin gate opening consistent with these co-evolved residues. **F**, Location of the T538-E652,

560   L545-T653, and L546-V457 residue pairs on PilQ[Pa] (left) and a model for secretin barrel folding

561   consistent with these co-evolved residues. **G,** Surface representation of conserved residues (top)

562   and electrostatic potential (bottom) in PilQ[Pa]. **H,** Structure alignment of monomers from the

563   spoked tetradecameric PilQ[Pa] (purple), tetradecameric PilQ[Pa] with no spokes (teal), and

564   pentadecameric PilQ[Pa] (orange) models. Grey square with black PilQ cartoon has a dotted red

565   box highlighting area of PilQ shown. Structural differences are highlighted (arrows) and the pivot

566   point for these differences is noted (black circle). **I,** Cartoon model summarizing the differences

567   between the three PilQ[Pa] structures determined. Pentadecameric PilQ[Pa] (orange) is wider and has

568   more horizontal secretin gates compared to the other structures. Tetradecameric PilQ[Pa] (teal) has

569   invaginated secretin gates and partial plug density (black triangle). Spoked tetradecameric PilQ[Pa]

570   (purple) has further invaginated secretin gates, plug density (black triangle), and spokes (black

571   circles).

572

573   **Figure 2. TsaP can be modeled in the PilQ spoke density as a heptameric ring. A,** TsaP

574   domain model predictions: the I-Tasser prediction of the CI domain (residues 126-211)[34] and the

575   Phyre[2] prediction of the CII domain (residues 235-324)[33]. **B,** Evolutionarily coupled residues in

576   TsaP (gray) are compared with the structure of the C-terminal 224 residues of TsaP. Residue

577   pairs that are within 8 Å of each other are shown from the CI domain (yellow), the CII domain

578   (wheat-yellow), and the linkers preceding and following the CI domain (brown). Intramolecular

579   and intermolecular contacts in the TsaP structure between the CI and CII domains are also shown

580   (blue and red, respectively). **C-D,** Map (top), model (middle), and cartoon (bottom) summarizing

581   the structure of TsaP. Zoomed-in (**C**) and zoomed-out (**D**) views are shown. TsaP is coloured as

582   in **B**; PilQ is shown in grey (**C**) or purple (**D**).

583

584   **Figure 3. TsaP over-expression induces cyclic di-GMP up-regulation.** Wild-type *P. aeruginosa*

585   (left), the *tsaP* mutant (center left), *P. aeruginosa* expressing TsaP (center right), and the *tsaP*

586   mutant expressing TsaP (right). **A,** Twitching motility was assayed by crystal violet staining and

587   the areas traversed by the bacteria were measured (violin plot with individual measurements shown

588   as empty circles; n = 7 for Wild-type with and without vector, n = 6 for the *tsaP* mutant with and

589   without vector; data are representative of three independent trials). Mean twitching areas were

590   compared to wild type plus the control vector at the corresponding arabinose concentration with

591   the two-way ANOVA test; p-values are reported. **B**, Representative crystal violet stained twitching

592   motility zones (top), Congo-red agar colonies (middle), and skim milk agar colonies (bottom) are

593   shown for 0 % arabinose induction (-) or 0.1% arabinose induction (++). **C**, Luminescence over

594   time relative to uninduced control without arabinose (top), with luciferase expression under the

595   control of the cyclic di-GMP inducible *cdrA* promotor. Mean luminescence (n=3, representative of

596   three independent trials) relative to a matched uninduced control is shown for 0.1% arabinose

597   induction (orange, ++) or 0.01% arabinose induction (beige, +) as a filled in line with the standard

598   error of the mean (dotted lines). Growth measured by absorbance at 600nm over time of liquid

599   cultures (bottom). Mean growth (n=3, representative of three independent trials) is shown for 0 %

600   arabinose induction (gray, -), 0.01% arabinose induction (beige, +), or 0.1 % arabinose induction

601   (orange, ++) with the standard error of the mean shown (dotted lines). **D**, Congo red dye uptake

602   assay of PAO1 (wild-type), PAO1::*pilN*, PAO1::*pilO*, PAO1::*pilP*, PAO1::*pilQ*, PAO1::*pilA*,

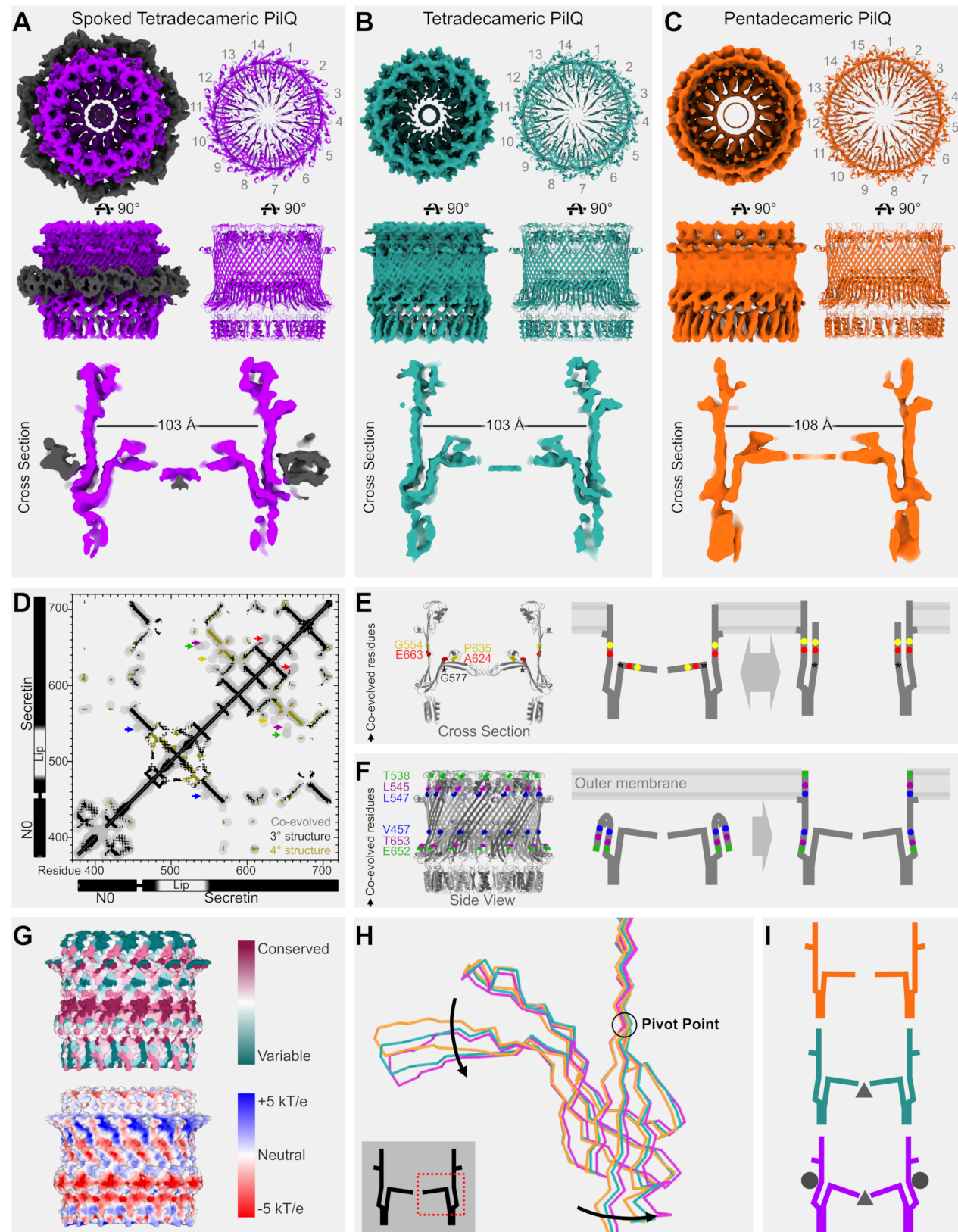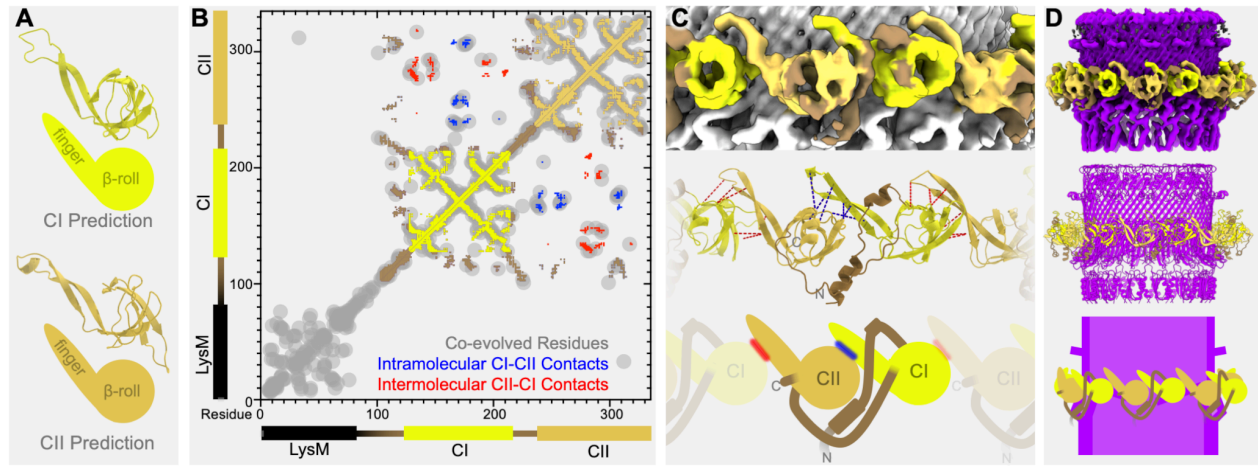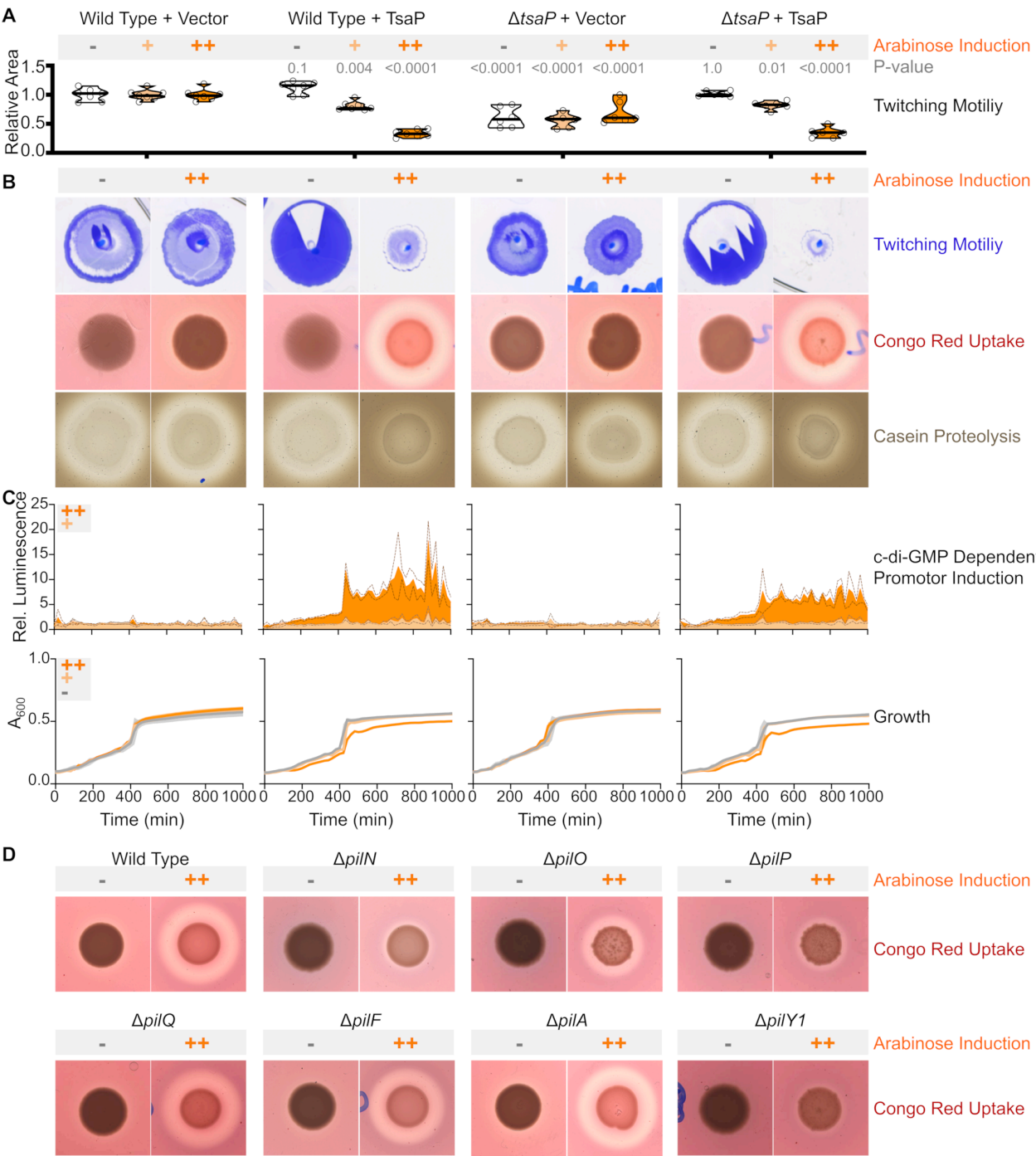603   PAO1::*pilF* and PAO1::*pilY1* with (++) and without (-) TsaP overexpression.

604

605

606

607   Figure 1

608

Figure 2

612   Figure 3

613